Optical Design of PICO, a Concept for a Space Mission to Probe Inflation and Cosmic Origins

Karl Young[a†], Marcelo Alvarez[b], Nicholas Battaglia[c], Jamie Bock[d], Jullian Borrill[e], David Chuss[f], Brendan Crill[g], Jacques Delabrouille[h], Mark Devlin[i], Laura Fissel[j], Raphael Flauger[k], Daniel Green[l], Kris Gorksi[g], Shaul Hanany[a], Richard Hills[m], Johannes Hubmayr[n], Bradley Johnson[o], Bill Jones[c], Lloyd Knox[p], Al Kogut[q], Charles Lawrence[g], Tomotake Matsumura[r], Jim McGuire[g], Jeff McMahon[s], Roger O'Brient[g], Clem Pryke[a], Brian M. Sutin[g], Xin Zhi Tan[a], Amy Trangsrud[g], Qi Wen[a], and Gianfranco de Zotti[t]

[a]University of Minnesota, USA
[b]University of California Berkeley, USA
[c]Princeton University, USA
[d]California Institute of Technology, USA
[e]Lawrence Berkeley National Laboratory, USA
[f]Villanova University, USA
[g]Jet Propulsion Laboratory, California Institute of Technology, USA
[h]Laboratoire AstroParticule et Cosmologie and CEA/DAP, France
[i]University of Pennsylvania, USA
[j]National Radio Astronomy Observatory, USA
[k]University of California San Diego, USA
[l]University of Toronto, Canada
[m]Cavendish Laboratory, University of Cambridge, UK
[n]National Institute of Standards and Technology, USA
[o]Columbia University, USA
[p]University of California Davis, USA
[q]Goddard Space Flight Center, USA
[r]Kalvi IPMU, University of Tokyo, Japan
[s]University of Michigan, USA
[t]Osservatorio Astronomico di Padova, Italy

ABSTRACT

The Probe of Inflation and Cosmic Origins (PICO) is a probe-class mission concept currently under study by NASA. PICO will probe the physics of the Big Bang and the energy scale of inflation, constrain the sum of neutrino masses, measure the growth of structure in the universe, and constrain its reionization history by making full sky maps of the cosmic microwave background with sensitivity 70 times higher than the Planck space mission. With bands at 21-799 GHz and arcmin resolution at the highest frequencies, PICO will make polarization maps of galactic synchrotron and dust emission to observe the role of Galactic magnetic fields in galactic evolution and star formation. We describe the current state of the PICO instrument design. We discuss the choice of optical system, which is based on an open-Dragone telescope that, to our knowledge, has not been used for mm-wave astrophysical observations. We also present the focal plane design, a white noise model of the instrument, and the expected noise level.

did you review the abstract? does it accurately represent the contents of the paper? Is it highlighting the unique and new things you are reporting? Is it quantitative? In order; yes, yes, I think so, and somewhat.

†E-mail: kyoung@astro.umn.edu, Telephone: 1 612 626 9149

need to distinguish between Current Best Estimate and Required Sensitivity. Added one sentence on this at end of 1st paragraph of intro. Does it need to be more prominent?

Keywords: Cosmic microwave background, cosmology, mm-wave optics, polarimetry, instrument design, satellite, mission concept

1. INTRODUCTION

Over the last decade NASA's astrophysics division has funded design and construction of space missions that are either Explorer-class, with cost cap of $\leq$ \$250M or Flagship-class that cost above \$1B. To study the science opportunities available at intermediate costs, NASA initiated studies of Probe-class missions with cost window between \$400M and \$1B. We are conducting one these studies for a mission called the Probe of Inflation and Cosmic Origins (PICO). A paper by Sutin et al.[1] in these proceedings gives an overall review of PICO and the scientific motivation. This paper describes the design of the telescope and focal plane and gives our current best estimate for the sensitivity of the instrument. The mission study is not complete; the final report is due in December 2018. Therefore, the quantitative assessments we provide are temporary in nature and subject to revision. Even so, the design is fairly mature and we do not expect significant changes. Values in this paper, such as component temperatures and detector noise levels, are current best estimates. They are not finalized mission requirements.

2. MISSION AND SPACECRAFT

PICO will conduct scientific observations for five years from an orbit around the Earth-Sun L2 Lagrange point. It has 21 bands centered at 21–799 GHz. The spacecraft design impacts the optical design and sensitivity in two primary ways; volume constraints limit the physical size of the telescope and optical component temperatures impact noise levels.

The maximum diameter of the spacecraft is limited by the SpaceX's Falcon 9 launch vehicle, which carries payloads up to 4.6 m in diameter. This diameter limits the V-groove shields' size, which, along with the scan strategy, defines the 'shadow cone' in Figure 1. The shadow cone is the volume protected from solar illumination, and all optical components must remain within it. The shadow cone and inner V-grooves define an available volume for the telescope. We opted not to use deployable shields as they presented added costs and risk which outweighed the benefits. The current thermal model indicates the temperatures of the optical elements as given in Figure 1. The primary reflector is passively cooled, while the optics box, secondary reflector, and focal plane are actively cooled; Sutin et al.[1] gives more details of the thermal system.

3. OPTICAL SYSTEM

The choice of telescope design was driven by a combination of science requirements and the physical limits discussed in Section 2. The science requirements were: a large diffraction limited field of view (DLFOV)[*] sufficient to support $\mathcal{O}(10^4)$ detectors, arcminute resolution at 800 GHz, low instrumental polarization, and low sidelobe response. Additionally, the transition edge sensor bolometers baselined for PICO require a telecentric focal plane which is sufficiently flat that it can be tiled by 10 cm detector wafers without reduction in optical quality.

To increase aperture efficiency and reduce sidelobes we concentrated on off-axis optical designs. More than 30 years ago Dragone analyzed the performance of several off-axis systems and found solutions with low cross-polarization at the center of the field of view and with astigmatism, or astigmatism and coma, canceled to first order.[2–4] These systems also had no cross-polarization at the center of the field of view. A number of recent CMB instruments used off-axis systems, and several began the design optimization with systems based on designs by Dragone.[5–10] For PICO we began the optimization with a two-reflector Dragone system that, to our knowledge, has not been implemented in CMB instruments before. We call it an 'open-Dragone' because of its overall geometry and in contrast to the widely used 'cross-Dragone', see Figure 3. We used a 1.4 m entrance aperture as this aperture diameter satisfied the science requirements.

[*] We consider an area in the FOV diffraction limited when the Strehl ratio is larger than 0.8.

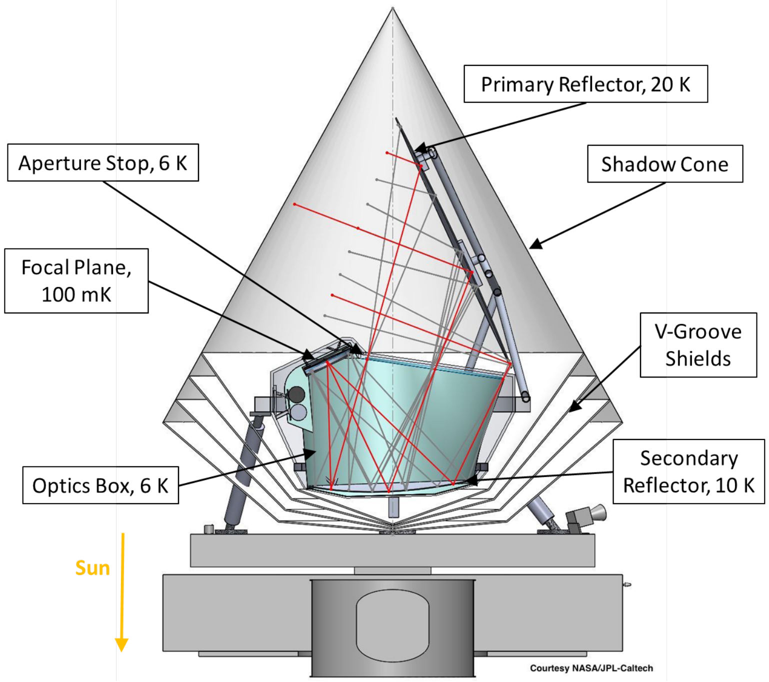

Figure 1. ~~Mechanical design of the PICO satellite. Components relevant to this paper are labeled, for other details see Sutin et al.[1]~~ The symmetry axis of the satellite precesses around the satellite-sun axis (orange arrow) with an angle of 26 deg figure is confusing; show the spin axis; show the sun along the shadow cone; show the boresight explicitly; show the 26 and 69 degrees. This precession defines the shadow cone which is shown in light gray.

We considered two additional Dragone systems, a Gregorian Dragone and a cross-Dragone, and compared the relative performance of all three systems in terms of DLFOV, compactness, and rejection of sidelobes. Compared to the open-Dragone, the Gregorian had half the DLFOV for the same F-number and could not support $\mathcal{O}(10^4)$ detectors. It was therefore rejected. The cross-Dragone had roughly $4\times$ the DLFOV of the open-Dragone, but was more difficult to pack inside the spacecraft volume while avoiding the known sidelobes shown in Figure 2. We found that the largest cross-Dragone which meets the PICO volume constraints had a 1.2 m aperture and an F-number of 2.5, while the largest open-Dragone aperture was 1.4 m with an F-number of 1.42. The larger F-number of the cross-Dragone system implied a larger physical focal plane, and therefore higher mass and cost, for the same number of pixels. For the PICO case, we concluded that the advantages of a low F-number and easily baffled sidelobes made the open-Dragone a good starting point for further optimization.

We designed the initial open Dragone following Granet's method.[11] We began with a solution with $F = 1.42$, a 1.4 m aperture (that was verified to satisfy the volume constraints), and a large DLFOV. We forced a circular aperture stop between the primary and secondary reflectors and numerically optimized its angle and position to obtain the the largest DLFOV. The stop diameter was chosen such that, for the center feed, it projected a 1.4 m effective aperture onto the primary. Adding a stop in this way increased the size of the primary reflector, because different field angles illuminated different areas on the reflector. Actively cooling the aperture stop, however, reduced detector noise, and the stop shielded the focal plane from stray radiation. At this stage the system still met the Dragone condition and is defined by the 'Initial Open-Dragone' parameters in Table 1.

In his publications Dragone provides a prescription to eliminate coma in addition to the cancellation of astigmatism provided by the baseline designs.[3] The corrections involve adding distortions to the primary and secondary reflectors which are proportional to r^4 where $r = 0$ is at the chief ray impact point on each reflector. We thus attempted to increase the DLFOV using two methods.

In 'Method1', one of the coauthors (RH) used Zemax to add Zernike polynomials to the base conics which described the reflectors. These Zernike polynomials were offset from the symmetry axis of the conic by 624.2 cm

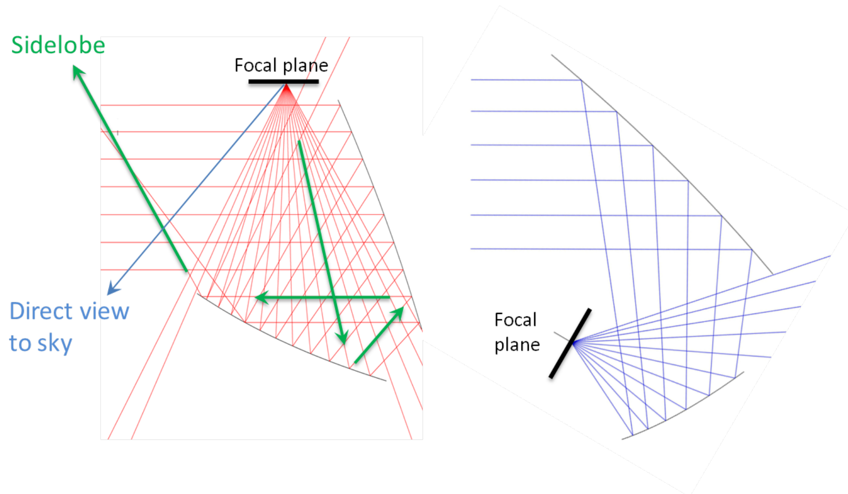

Figure 2. Comparison of sidelobes for a cross-Dragone (left) and an open-Dragone (right) please add labels to Figure as well. Rays are traced from the center of the focal plane toward the sky same angular opening of rays?. For both systems spillover around the secondary is straightforward to mitigate with absorptive baffles show sketch of such baffles?. However, the rays labeled 'sidelobe' and 'direct view to sky' in the cross-Dragone system present added challenges. The challenges can be mitigated—with a long forebaffle or larger F-number (see for example Matsumrua et al.[9]—but doing so increases the overall physical size of the system, which is problematic in the PICO case.

for the primary and 76.1 cm for the secondary. This placed the origin of polynomials at the chief ray impact point for each reflector. Inspired by the Dragone corrections, all Zernike terms up to fourth order and the first fifth order term were allowed to vary. The optimization metric was minimization of the rms spot diameter at the following locations: the center of the FOV, ± 2 deg in Y, and ± 4 deg in X. The center of the FOV was given a weight of 100 while each outer point was given a weight of 1. To constrain the optimization, the X and Y effective focal lengths were held fixed as was the impact point of the chief ray on the focal plane. This optimization step increased the DLFOV by factors of 1.15, 2.4 and 10.5 at 21, 155 and 799 GHz, respectively. We further increased the DLFOV by approximately 50% at all frequencies by including a curved focal surface and rerunning the optimization. A small ($\sim$4%) additional gain in DLFOV was achieved by adding Zernike terms up to sixth order, allowing the secondary to focal surface distance to vary, adding a weighted constraint on the effective focal length, and adding fields with weight of 0.01 to the rms spot diameter metric at ± 7.5 deg in Y and $+15$ deg in X. These additional fields were necessary to constrain the corrections at the reflector edges.

In 'Method2' another coauthor (JM) used CodeV and allowed additional geometric parameters of the system to vary. To adjust the reflector shapes, we added Zernike polynomial corrections to the conic surfaces which defined the two reflectors. The Zernike polynomials were defined in the same coordinate systems as the base conics. We varied the 4th and 9th-13th Zernike coefficients. We allowed the focal surface curvature and focal surface to secondary distance L_s to vary. The primary-secondary distance L_m, primary offset h, and the primary and secondary rotation angles, α and β, were varied as well. The optimization metric was the rms spot diameter across the field of view, with weighted constraints requiring telecentricity and maintaining the X- and Y-focal lengths. We added Lagrange constraints to enforce beam clearances and place an upper limit on overall system size. Once the optimization converged to an acceptable optical system, we added higher order Zernike terms, 19th-25th, and refined the reflector shapes using the same metric and constraints. The current PICO optical design is from the Method2 optimization procedure.

Figure 4 shows that Method2 greatly increased the DLFOV relative to the initial open-Dragone design. The DLFOV increased by factors of 1.9, 3.8, 4.3, and 4.6 at 21, 129, 155, and 799 GHz, respectively. The most important gain was at frequencies of 129 and 155 GHz. We used this extra area to add more C and D pixels, see Figure 5 and Section 4. The C and D pixels contained the bands most sensitive to the CMB, and adding hundreds of these pixels into the focal plane gave PICO unprecedented levels of CMB sensitivity. Method2 gave

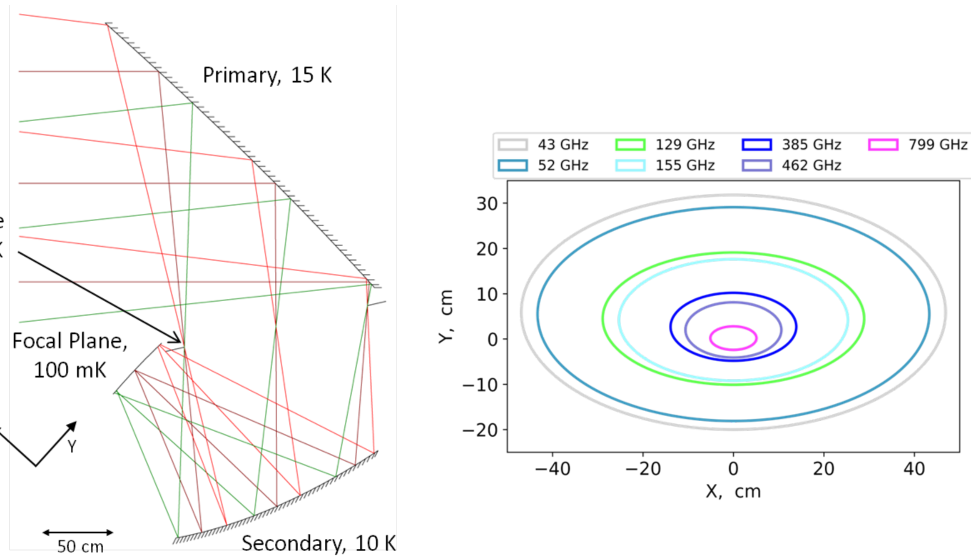

Figure 3. Raytrace (left) and Strehl = 0.8 contours (right) for the PICO optical design.

Table 1. Telescope geometric parameters ADD F# to Table

PICO optical system					Initial Open-Dragone[b]	
	Primary	Secondary	Telescope parameters[b]		Fundamental design parameters	
Reflector size[a] (cm)	270 × 205	160 × 158	Aperture (cm)	140	Aperture (cm)	140
Radius of curvature (cm)	∞	136.6	F-number	1.42	θ_0 (deg)	90
Conic constant, k	0	-0.926	h (cm)	624.2	θ_e (deg)	20
Normalization radius (cm)	524.8	194.1	α (deg)	74.2	θ_p (deg)	140
4th Zernike Coefficient (cm)	2018.4	-61.1	β (deg)	62.3	L_m (cm)	240
9th Zernike Coefficient (cm)	-37.0	16.7	L_m (cm)	229.3		
10th Zernike Coefficient (cm)	-2919.8	-15.1	L_s (cm)	140.5	Derived parameters	
11th Zernike Coefficient (cm)	-1292.7	22.3			F-number	1.42
12th Zernike Coefficient (cm)	120.6	-3.8	Focal Surface		h (cm)	624.2
13th Zernike Coefficient (cm)	-74.5	4.9	Ellipse major axes (cm)	69 x 45	α (deg)	38.6
19th Zernike Coefficient (cm)	-75.8	3.4	Ellipse major axes (deg)	19 x 13	β (deg)	101.4
20th Zernike Coefficient (cm)	-398.9	6.3	Radius of curvature (cm)	455	L_s (cm)	122.2
21st Zernike Coefficient (cm)	-319.5	23.3			Primary, f (cm)	312.1
22nd Zernike Coefficient (cm)	-276.6	-8.5			Secondary, a (cm)	131
23rd Zernike Coefficient (cm)	-201.6	-3.2			Secondary, e	1.802
24th Zernike Coefficient (cm)	-127.4	-1.9				
25th Zernike Coefficient (cm)	-55.0	0.1				

[a] The maximum physical size of the reflectors.
[b] Telescope parameters follow the definitions in Granet 2001.[11]

somewhat better performance at lower frequencies with a DLFOV 1.11 and 1.15 times larger than Method1 at 21 and 155 GHz, respectively. At 799 GHz Method2 gave DLFOV only 0.3 times that of Method1's area, but the DLFOV still satisfied our science requirements. Figure 4 also shows that Method2 reduced the overall telescope volume and gave more physical margin relative to the shadow cone.

The geometric parameters of the PICO optical system are given in Table 1. The system was diffraction limited for 799 GHz at the center of the field of view. At 155 GHz the DLFOV was 82.4 deg^2 and the total throughput at 20 GHz was 910 cm^{2}sr. Figure 3 shows Strehl of 0.8 contours for all pixel types. The slightly concave focal surface, which had a radius of curvature of 4.55 m, was telecentric to within 0.12 deg across the entire FOV.

An additional benefit of the optimization was the concave focal surface. The open-Dragone's focal surface is

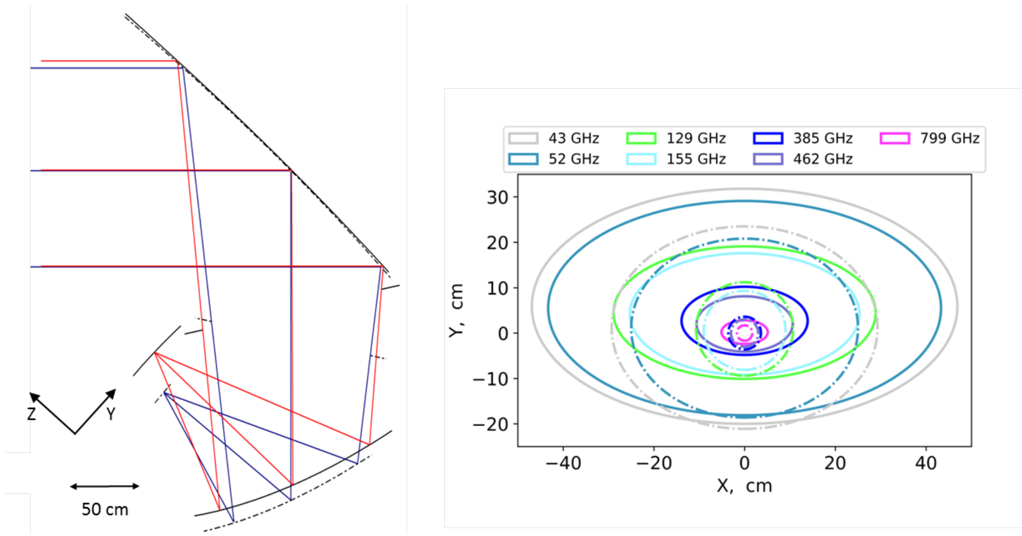

Figure 4. Comparison between the open-Dragone optimized using method two and the initial open-Dragone. The ray traces (left) are aligned at the chief ray impact point on the primary. The final optical system, optimized with Method2 (red rays, solid reflectors), is smaller in the vertical direction than the unoptimized version original dragone or Method1? (blue rays, dash-dot reflectors). The overlaid Strehl = 0.8 contours (right) show the improvement at all frequencies in the optimized (solid lines) system over the unoptimized (dash-dot lines) system. same question? Perhaps show all three options?

naturally curved. Matching this curvature reduced defocus, increased the DLFOV, and increased telecentricity. The unoptimized system was telecentric to within 2.5 deg while the optimized version was telecentric to within 0.12 deg. If the focal surface was too strongly curved tiling it with flat detector wafers would result in large defocus at the edges of these wafers. This was not the case for PICO. The focal surface radius of curvature, 4.55 m, resulted in a defocus of 0.1 mm at the edge of a 10 cm wafer.

4. FOCAL PLANE

Modern mm/sub-mm bolometers are photon noise limited. An effective way to increase sensitivity is to increase the number of detectors in the focal surface. The PICO focal ~~plane~~ surface has 12,996 detectors, 175 times the number flown on *Planck*. PICO achieves this by having a large DLFOV and using multichroic pixels (MCPs).[12,13] The MCP architecture assumed for PICO has three bands per pixel with two single polarization transition edge sensor (TES) bolometers per band and therefore six bolometers per pixel. We assume the MCPs are coupled to free space using lenslets and sinuous antennae,[12] but the focal plane layout, including pixel sizes, numbers, and spacing would not change significantly if horn or phased array coupling was used instead.

PICO has 21 overlapping bands with centers spanning the range 21–799 GHz. The bands are divided amongst nine pixel types labeled A to I; see Figure 5. The 25% fractional bandwidth is broader than the interband spacing causing neighboring bands to overlap and requiring them to be in separate pixels. The exceptions to the MCP architecture are the highest three bands, because they are above the superconducting band gap of niobium which is used for the transmission lines, antennae, and filters of the MCPs. For bands G, H, and I, we will use feedhorn-coupled polarization sensitive bolometers. The technology has high TRL as it has already been used successfully with *Planck*[14] and Herschel SPIRE.[15]

Figure 6 shows the PICO focal plane. We optimize the diameter of each MCP by calculating the array sensitivity for that pixel type. The calculation includes the increased illumination of the aperture stop as the pixel diameter decreases, as described in Section 5.1. We choose a pixel diameter of $2.1F\lambda_{\mathrm{mid}}$, where λ_{mid} refers to the center band of each pixel. This gives an edge taper, T_e, on the stop of 10 dB for the center band of each pixel.

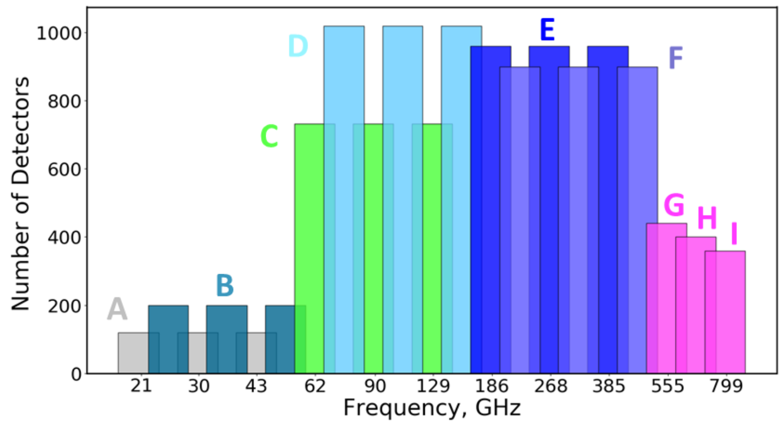

Figure 5. Frequency coverage of the PICO bands. Each color (excluding magenta) denotes a different MCP, labeled A-F. The bar height indicates the number of detectors per band. Bar width gives the bandwidth. All bands are top-hats with 25% fractional bandwidth; the x-axis is logarithmic. The three highest frequencies (magenta) are the single color pixels G, H, and I.

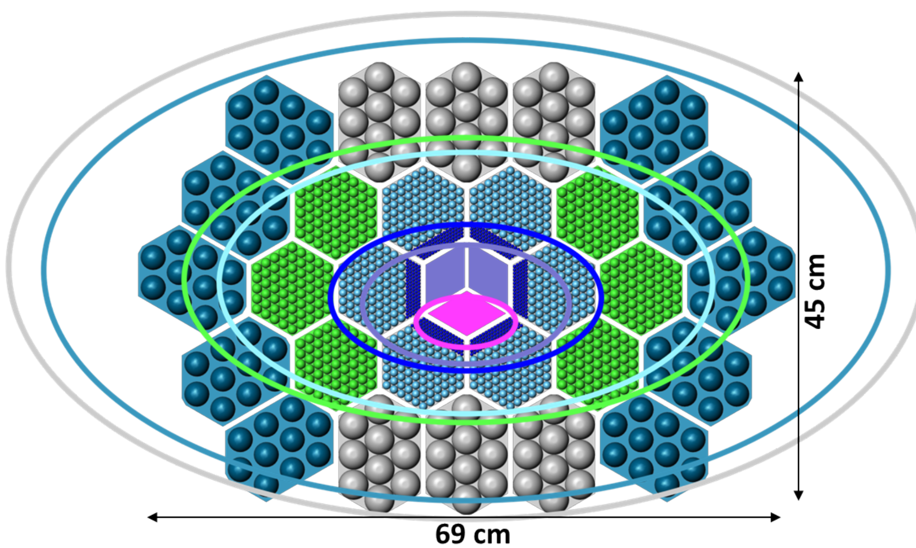

Figure 6. PICO focal plane layout with Strehl = 0.8 contours for each pixel type. The pixel and Strehl contour colors match the band colors, A-I, in Figure 5

Differencing detectors that are sensitive to orthogonal polarization states enables each pixel to make a measurement of a particular Stokes parameter. Pixels that are sensitive to the U Stokes parameter are rotated by 45 deg relative to those that are sensitive to Q. This Q/U measurement is in the instrument reference frame with the x-axis parallel to the scan direction; see Figure 7. combine Figures 6 and 7 together?

The PICO focal plane readout has been designed around ×128 time domain multiplexing (TDM), but this choice is not a significant driver for the focal plane layout or overall noise budget.

5. INSTRUMENT NOISE

We develop past tense here and throughout please an end to end noise model of the PICO instrument to predict full mission sensitivity and provide a metric by which to evaluate mission design trade-offs. This model assumes

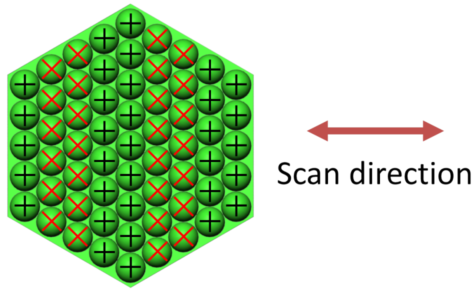

Figure 7. Layout of pixels sensitive to Stokes Q (black crosses) and Stokes U (red exes) for an example wafer.

white noise at all frequencies. The overall sensitivity does not include calibration uncertainties or estimates of other possible systematic effects. To construct the model we estimate the optical load, calculate noise equivalent power (NEP) by source, combine all NEP terms to get detector noise, combine all detectors to get noise per frequency band, and then include total mission time to find overall mission sensitivity.[16,17] Each of these steps includes various assumptions and design decisions, which are discussed in this section. The assumptions are summarized in Table 2. The values presented here are our current best case estimates. Instrument noise *requirements*, which would have larger noise levels, are still being determined.

To validate our model we compared two independent calculations using codes that were used for several earlier CMB instruments. The calculations agree within 1% for individual noise terms and for overall mission noise. We also use our model to calculate CORE and LiteBIRD noise using their published system parameters. The results are consistent with published values when similar assumptions are used. move these to later; let's talk on the phone Additionally, we compare PICO detector noise to CORE and LiteBIRD detector noise. The lower PICO noise is explained by the cold system and differing optical efficiency. From these test we conclude that our model is correct and our assumptions are reasonable.

Table 2. Noise model parameters, see text for details.

Throughput	single moded, λ^2
Fractional Bandwidth	25%
Reflector emissivity	$\epsilon = \epsilon_0\sqrt{\nu/150\text{ GHz}}, \epsilon_0 = 0.07\%$
Aperture stop emissivity	1
Low pass filter reflection loss	8%
Low pass filter absorption loss[a]	frequency dependent, 0.2%–2.8%
Bolometer absorption efficiency	70%
T_e of low, middle, and high bands (dB)	4.8, 10.0, 20.7
η_{stop} of low, middle, and high bands	0.68, 0.90, 0.99
Bose noise fraction, ξ	1
Bolometer yield	90%
Bath temperature, T_o (mK)	100
TES critical temperature, T_c (mK)	187
Safety factor, $P_{\text{sat}}/P_{\text{abs}}$	2
Thermal power law index, n	2
Intrinsic SQUID noise (aW/$\sqrt{\text{Hz}}$)	3
TES operating resistance, Ω	0.03
TES transition slope, α	100
TES loop gain	14
Mission length (years)	5
Observing efficiency	95%

[a] Assumes different thickness per pixel.

5.1 Single bolometer noise

5.1.1 Model

The sources of optical load are the CMB, the primary and secondary reflectors, the aperture stop, and low pass filters. These elements are shown schematically in Figure 8. The total load absorbed at the bolometer is the sum of the power emitted by each element reduced by the transmission efficiency of the elements between the emitting surface and the bolometer. The absorbed power is

$$P_{\rm abs} = ((((P_{\rm CMB}\eta_{\rm PRI} + P_{\rm PRI})\eta_{\rm stop} + P_{\rm stop}(1-\eta_{\rm stop}))\eta_{\rm SEC} + P_{\rm SEC})\eta_{\rm filter} + P_{\rm filter})\eta_{\rm bolo}, \quad (1)$$

where $P_{\rm elem}$ is the in band power emitted by a given element for a single polarization and $\eta_{\rm elem}$ is the transmission efficiency of the element. Power emitted by the stop is a special case. We multiply $P_{\rm stop}$ by $(1-\eta_{\rm stop})$ because $\eta_{\rm stop}$ is the spillover efficiency, the fraction of the throughput which passes through the stop. Therefore $(1-\eta_{\rm stop})$ is the fraction of the throughput which views the stop. We determine $\eta_{\rm stop}$ in the following way. The MCP angular beam width depends on the wavelength and pixel diameter as[16]

$$\theta_{1/e^2} = \frac{2.95\lambda}{\pi D_{\rm px}}. \quad (2)$$

please check We fix $D_{\rm px}$ such that the edge taper T_e of the middle frequency band in each pixel is 10 dB and calculate T_e for the upper and lower bands using Equation 2. This changing illumination of the stop is shown schematically by the dashed rays in Figure 8. For each MCP in pixels A-H T_e is 4.8, 10, and 20.7 dB for the lower, middle, and upper bands, respectively. These edge tapers correspond to $\eta_{\rm stop}$ of 0.68, 0.90, and 0.99. The changing $\eta_{\rm stop}$ has two main effects; changing optical efficiency between bands, which affects optical load and the NEP to noise equivalent temperature (NET) conversion, and telescope beam size not scaling smoothly with λ. The left panel of Figure 9 gives the optical load as a function of frequency. The jumps in load between neighboring bands near 70 and 200 GHz, are due to $\eta_{\rm stop}$ changing with frequency, comma was missing. I believe that in most cases a comma precedes 'which' which is a consequence of using MCPs.

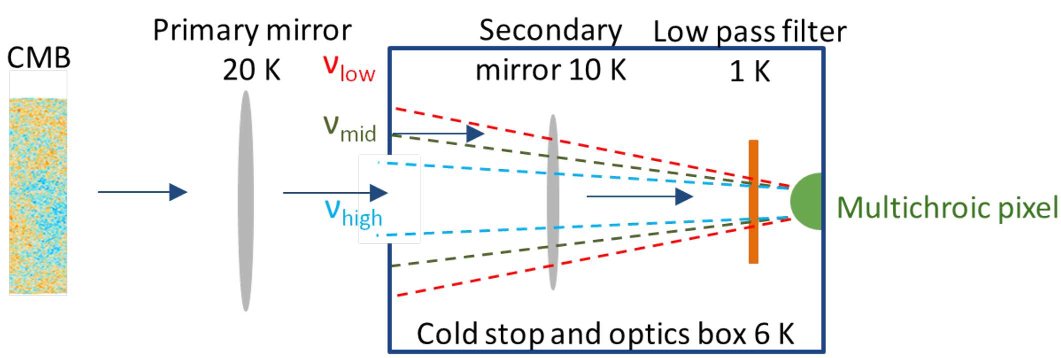

Figure 8. Schematic representation of the prediction of optical load. Power emitted by each element is modified by the efficiency of the following elements and added to the total expected load. The multichroic pixel illuminates the stop differently for each of the three bands.

We consider four noise sources per bolometer; photon, phonon, TES Johnson, and readout. Photon noise depends on the absorbed power,[18]

$$NEP_\gamma^2 = \int_{\rm band} 2h\nu p_\nu \, d\nu + 2\xi \int_{\rm band} p_\nu^2 \, d\nu, \quad (3)$$

where p_ν is the power spectral density for a single polarization absorbed at the bolometer and $\xi = 1$ is the fraction of correlated Bose photon noise. We include a factor of 2 in the Bose noise term because the bolometers

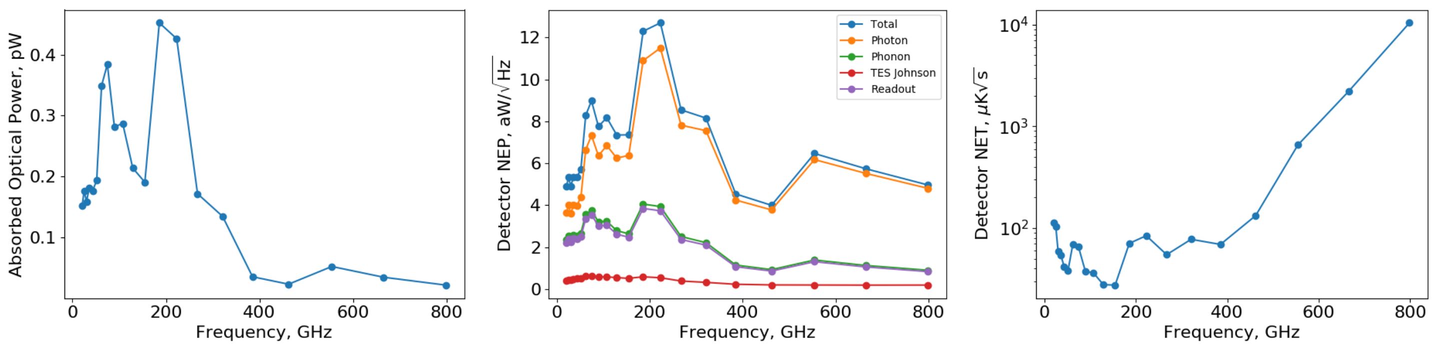

Figure 9. Left: Expected optical load as a function of frequency for single polarization PICO bolometers. Center: Breakdown of NEP sources across the PICO frequency range. Photon noise dominates even at the lowest frequencies. Right: Single detector NET for the PICO bands.

receive the power from a single polarization. From $P_{\rm abs}$ we calculate the TES bolometer properties and phonon noise.[19] We calculate TES Johnson noise, which depends on bolometer bias parameters, for each frequency band. All noise sources in the cold and warm readout electronics are lumped under the readout term. The combined NEP and for each noise source as a function of frequency are shown in Figure 9; the combined value is given in Table 3. did you even define the term NEP?

5.1.2 Results

~~For PICO~~ The primary contributor to noise is the optical load. The CMB and stop account for the majority of the optical load at all frequencies. Even at 800 GHz the CMB and stop account for 12% more power than the reflectors; show components in the Figure? see the left panel of Figure 9. is the following consistent with the previous sentence? The load from the reflectors is greatest at 799 GHz where it is 47% of the total optical load. The CMB provides more than half the load in the middle and upper bands of the multichroic pixels, but the stop dominates the load in the lowest band of each pixel. Load from the stop in the lowest band of each pixel ranges from 1.2 times the CMB load at 21 GHz to a maximum of 4.7 times the CMB load at 223 GHz. did we consider two bands per pixel?

Bose noise is most significant at lower frequencies with $\mathrm{NEP_{Bose}}/\mathrm{NEP_{Poisson}} = 1.5$ in the lowest band. (All NEP ratios are calculated using units of $\mathrm{W}/\sqrt{\mathrm{Hz}}$ for the dividend and divisor.check) However, Poisson noise increases as $\sqrt{P_{\rm abs}\nu}$ while Bose is proportional to $P_{\rm abs}$. The Poisson noise equals Bose noise at 30 GHz and dominates at higher bands; $\mathrm{NEP_{Bose}}/\mathrm{NEP_{Poisson}} < 10\%$ at 321 GHz. Phonon noise is the second most significant source, $\mathrm{NEP_{phonon}}/\mathrm{NEP_{photon}}$ ranges from 65% at 21 GHz to 19% at 799 GHz.

For TDM readout, phonon and readout noise are ~~roughly~~ approximately equal with TES Johnson noise being insignificant. We also modeled noise for frequency domain multiplexing readout (FDM). For FDM the TES Johnson noise is higher, 2/3 of the readout NEP, but the readout noise is lower. Comparing the combined TES Johnson and readout NEPs for TDM and FDM we find essentially identical performance with total noise differing by less than 3% across all bands. For both systems we require a focal plane temperature, T_o, of 100 mK and a bolometer safety factor of 2 to remain photon noise dominated at the lowest bands. what does this mean? that if the safety factor is higher we are not photon noise dominated?

5.2 Combined array noise

Using single detector NEPs from Section 5.1 and the detector counts from Section 4 we calculate the combined NEP of the detector array for each band. Combining detectors simply reduces noise by $\sqrt{N}$ except for Bose photon noise. ~~For the lowest band of each MCP the pixels over sample the PSF, pixel spacing is 0.4Fλ, resulting in correlated Bose noise between pixels.~~ have you defined psf? spell out. Also please avoid this style: fragment, explaining the fragment, fragment. For the lowest band of each MCP the pixel spacing is 0.4Fλ and thus the pixels oversample the point spread function leading to correlated photon noise between pixels. Accounting for this effect gives a 26% increase in the combined array NEP for the 21 GHz band ~~of the lowest frequency band, 21 GHz,~~ fragment, explain, fragment and a 0.003% increase ~~in array NEP~~ at ~~the highest band,~~ 799 GHz.

From the array NEP we convert to noise equivalent temperature NET per band~~,~~ using

$$\frac{NEP}{NET} = \sqrt{2}\,\eta_{\rm opt} \int\limits_{\rm band} \frac{dp_\nu}{dT}\Big|_{T_{\rm CMB}} d\nu. \tag{4}$$

The $\eta_{\rm opt}$ term contributes to the 'jumps' in NET seen in Figure 9, because $\eta_{\rm opt}$ varies band to band. Numerical values for the NET are given in the second to last column in Table 3.

Assuming evenly weighted observations of the full sky, 5 years of mission duration, and 95% efficiency, we calculate full mission map sensitivities in polarization; see the final column in Table 3. Karl, please don't replace words with punctuation marks. Use sentences with words. Combining all bands gives a total CMB map depth for the entire PICO mission of 0.62 μK$_{\rm CMB}$-arcmin.

Table 3. PICO frequency channels and noise.

Pixel Type	Band GHz	FWHM arcmin	Bolometer NEP aW/$\sqrt{Hz}$	Bolometer NET μK$_{\rm CMB}\sqrt{s}$	$N_{\rm bolo}$	Array NET μK$_{\rm CMB}\sqrt{s}$	Polarization map depth μK$_{\rm CMB}$-arcmin	Polarization map depth Jy/sr
A	21	38.4	4.89	112.2	120	13.6	19.2	6.69
B	25	32.0	5.33	103.0	200	9.56	13.5	7.98
A	30	28.3	4.92	59.4	120	5.90	8.31	7.93
B	36	23.6	5.36	54.4	200	4.17	5.88	9.59
A	43	22.2	5.33	41.7	120	4.01	5.65	13.9
B	52	18.4	5.73	38.4	200	2.86	4.03	16.8
C	62	12.8	8.29	69.2	732	3.13	4.42	37.0
D	75	10.7	8.98	65.4	1020	2.47	3.47	48.1
C	90	9.5	7.76	37.7	732	1.49	2.10	44.5
D	108	7.9	8.18	36.2	1020	1.21	1.70	57.0
C	129	7.4	7.35	27.8	732	1.09	1.53	69.7
D	155	6.2	7.36	27.5	1020	0.91	1.28	84.6
E	186	4.3	12.30	70.8	960	2.52	3.54	383
F	223	3.6	12.70	84.2	900	3.05	4.29	579
E	268	3.2	8.55	54.8	960	1.87	2.62	369
F	321	2.6	8.16	77.6	900	2.73	3.84	518
E	385	2.5	4.54	69.1	960	2.35	3.31	318
F	462	2.1	4.00	132.6	900	4.66	6.56	403
G	555	1.5	6.47	657.8	440	33.1	46.5	1569
H	666	1.3	5.74	2212	400	117	164	1960
I	799	1.1	4.97	10430	360	560	816	2321
Total					12996	0.46	0.65	

SH Here

6. CONCLUSIONS/SUMMARY

The PICO optical system is a simple two reflector open-Dragone which we numerically optimize to maximize the DLFOV. The addition of a cold aperture stop and cold reflectors minimize optical load and reduce noise. The focal plane takes advantage of the large DLFOV and MCP technology to implement 12996 polarization sensitive detectors in 21 bands from 21-799 GHz. When combining all bands, our instrument noise model predicts full mission polarization map depth of 0.62 μK$_{\rm CMB}$-arcmin.

7. ACKNOWLEDGMENTS

This Probe mission concept study is funded by NASA grant #NNX17AK52G. Gianfranco de Zotti acknowledges financial support from the ASI/University of Roma–Tor Vergata agreement n. 2016-24-H.0 for study activities of the Italian cosmology community. Jacques Delabrouille acknowledges financial support from PNCG for participating to the PICO study.

REFERENCES

[1] Sutin, B. M., Alvarez, M., Battaglia, N., et al., "PICO - the probe of inflation and cosmic origins," Proc. SPIE **10698** (2018).

[2] Dragone, C., "Offset multireflector antennas with perfect pattern symmetry and polarization discrimination," Bell Labs Technical Journal **57**(7), 2663–2684 (1978).

[3] Dragone, C., "First-order correction of aberrations in Cassegrainian and Gregorian antennas," IEEE Transactions on Antennas and Propagation **31**, 764–775 (September 1983).

[4] Dragone, C., "Unique reflector arrangement with very wide field of view for multibeam antennas," Electronics Letters **19**(25), 1061–1062 (1983).

[5] Fargant, G., Dubruel, D., Cornut, M., et al., "Very wide band telescope for Planck using optical and radio frequency techniques," in [UV, Optical, and IR Space Telescopes and Instruments], Breckinridge, J. B. and Jakobsen, P., eds., Proc. SPIE **4013**, 69–79 (July 2000).

[6] Swetz, D. S., Ade, P. A. R., Amiri, M., et al., "Overview of the Atacama Cosmology Telescope: Receiver, Instrumentation, and Telescope Systems," *ApJS* **194**, 41 (June 2011).

[7] Padin, S., Staniszewski, Z., Keisler, R., et al., "South Pole Telescope optics," *Appl.* Opt. **47**, 4418–4428 (Aug. 2008).

[8] de Bernardis, P., Ade, P. A. R., Baselmans, J. J. A., et al., "Exploring cosmic origins with CORE: The instrument," Journal of Cosmology and Astro-Particle Physics **2018**, 015 (Apr. 2018).

[9] Matsumura, T., Akiba, Y., Arnold, K., et al., "LiteBIRD: Mission Overview and Focal Plane Layout," Journal of Low Temperature Physics **184**, 824–831 (Aug. 2016).

[10] Parshley, S., Niemack, M., and Hills, R. E., "The optical design of the six-meter CCAT-prime and Simons Observatory telescopes," Proc. SPIE **10700** (2018).

[11] Granet, C., "Designing classical Dragonian offset dual-reflector antennas from combinations of prescribed geometric parameters," IEEE Antennas and Propagation Magazine **43**, 100–107 (Dec. 2001).

[12] Suzuki, A., Arnold, K., Edwards, J., et al., "Multi-chroic dual-polarization bolometric detectors for studies of the cosmic microwave background," Journal of Low Temperature Physics **176**, 650–656 (Sep 2014).

[13] Datta, R., Hubmayr, J., Munson, C., et al., "Horn Coupled Multichroic Polarimeters for the Atacama Cosmology Telescope Polarization Experiment," Journal of Low Temperature Physics **176**, 670–676 (Sept. 2014).

[14] Lamarre, J. M., Puget, J. L., Ade, P. A. R., et al., "Planck pre-launch status: The HFI instrument, from specification to actual performance," *A&A* **520**, A9 (Sept. 2010).

[15] Griffin, M. J., Abergel, A., Abreu, A., et al., "The Herschel-SPIRE instrument and its in-flight performance," *A&A* **518**, L3 (July 2010).

[16] Suzuki, A., Multichroic Bolometric Detector Architecture for Cosmic Microwave Background Polarimetry Experiments, PhD thesis, University of California, Berkeley (Jan. 2013).

[17] Aubin, F., Detector Readout Electronics for EBEX: A Balloon-borne Cosmic Microwave Background Polarimeter, PhD thesis, McGill University (2013).

[18] Richards, P. L., "Bolometers for infrared and millimeter waves," Journal of Applied Physics **76**, 1–24 (July 1994).

[19] Mather, J. C., "Bolometer noise: nonequilibrium thoery," *Appl.* Opt. **21**, 1125–1129 (Mar. 1982).